

GEOPHYSICS

Mesozoic intraoceanic subduction shaped the lower mantle beneath the East Pacific Rise

Jingchuan Wang^{1*}, Vedran Lekić¹, Nicholas C. Schmerr¹, Yu J. Gu², Yi Guo², Rongzhi Lin^{2*}

The Pacific large low-shear-velocity province (LLSVP), as revealed by cluster analysis of global tomographic models, hosts multiple internal anomalies, including a notable gap (~20° wide) between the central and eastern Pacific. The cause of the structural gap remains unconstrained. Directly above this structural gap, we identify an anomalously thick mantle transition zone east of the East Pacific Rise, the fastest-spreading ocean ridge in the world, using a dense set of SS precursors. The area of the thickened transition zone exhibits faster-than-average velocities according to recent tomographic images, suggesting perturbed postolivine phase boundaries shifting in response to lowered temperatures. We attribute this observation to episodes of Mesozoic-aged (250 to 120 million years ago) intraoceanic subduction beneath the present-day Nazca Plate. The eastern portion of the Pacific LLSVP was separated by downwelling because of this ancient oceanic slab. Our discovery provides a unique perspective on linking deep Earth structures with surface subduction.

INTRODUCTION

It has long been suggested that Earth's lower mantle is dominated by two broad regions of low shear velocities and excess density beneath the Pacific and Indo-Atlantic (1–4). These megastructures, known as large low-shear-velocity provinces (LLSVPs), are interpreted as reservoirs of primitive material (5) or subducted oceanic lithosphere (6). The LLSVPs exhibit strong degree 2 and 3 signatures (7). Finer-scale seismic imaging based on waveforms (8, 9) provides further evidence for sharp boundaries of the LLSVPs, suggesting a complicated morphology. Geodynamic simulations have attributed the geometry and stability of the lower mantle structures to their direct interactions with subducting slabs (10–12). According to the classic view, cold and dense material is driven by subduction history toward upwelling regions over the course of hundreds of millions of years (10).

It remains controversial whether LLSVPs represent compact, continuous piles of compositionally distinct material (10) or clusters of thermochemical plumes (13). Compared to the African LLSVP, the Pacific anomaly is less conclusive in terms of geographic extent and geometry due to sparse data coverage in vast oceanic regions. Earlier seismic tomographic models suggested that the Pacific LLSVP is composed of a bundle of plumes (1, 14), and this observation was reinforced by later generations of tomographic models such as SEMUCB-WM1 (15). On the basis of cluster analysis of tomographic models, the Pacific LLSVP can be divided into three distinct portions during its ascent to the midmantle: the West Pacific anomaly, the East Pacific anomaly, and a central superswell anomaly in the middle (16). The West Pacific anomaly is connected to a cone-shaped anomaly beneath the South Pacific superswell via a narrow corridor. This observation has been corroborated by waveform modeling of shear waves (*S/Sdiff*, *ScS*, and *SKS/SKKS*) (9). The easternmost anomaly, located east of the southern East Pacific Rise (SEPR), covers much of the Nazca Plate with a remarkable ~2000-km-wide gap, separating it from the superswell anomaly. The cause of this structural gap

remains undetermined, given the coarse resolution of most global tomographic models and the limited sampling of raypaths, both of which hamper regional-scale tomography.

Among tectonic plates, the Nazca Plate is unique in that it shares the world's fastest-spreading ocean ridge on its western boundary and the spatially longest continuous subduction zone along its eastern boundary. It also hosts several active hot spots, including the Easter hot spot that is postulated to represent a deep-rooted plume (17, 18), and the plate accommodates three microplates along the SEPR. Although studies have suggested that slabs can modify the LLSVP as they sink into the mantle, none have yet identified a subduction episode beneath the Nazca Plate that could account for the observed structural gap in the LLSVP. A key constraint on deciphering the potential interplay between slabs/upwellings and the mantle is the thickness of the mantle transition zone (MTZ), the region bounded by the 410- and 660-km discontinuities (hereafter referred to as the 410 and 660). Because of the postolivine phase transitions, the topography of the 410 and 660 has a strong dependence on temperature. Plume- and slab-MTZ interactions are expected to induce a thin and thick MTZ, respectively (19).

Here, we present high-resolution MTZ imaging beneath the SEPR and surrounding ocean basins by stacking an up-to-date dataset of SS precursors (Fig. 1 and fig. S1) (see Materials and Methods). These phases reflect off mantle discontinuities rather than the surface and are well known for providing sampling coverage under oceanic regions (fig. S1B). We seek to improve the resolution of these waves by stacking waveforms in 5°-radius caps and to reduce uncertainties by applying fast multichannel singular spectrum analysis (FMSSA) for prestack data regularization and noise suppression (see Materials and Methods for details). The resulting discontinuity structure is compared to mantle tomography observations (20) and plate reconstructions (21) to identify the source of the unusual structure beneath the region.

RESULTS

Overview of MTZ observations

Lateral variations in discontinuity depths are obtained by a cap-averaging scheme consisting of 336 overlapping circular caps of 5°

Copyright © 2024 The Authors, some rights reserved; exclusive licensee American Association for the Advancement of Science. No claim to original U.S. Government Works. Distributed under a Creative Commons Attribution NonCommercial License 4.0 (CC BY-NC).

¹Department of Geology, University of Maryland, College Park, MD 20742, USA.

²Department of Physics, University of Alberta, Edmonton, Alberta T6G 2E1, Canada.

*Corresponding author. Email: jingchuan@ualberta.ca (J.W.); rongzhi@ualberta.ca (R.L.)

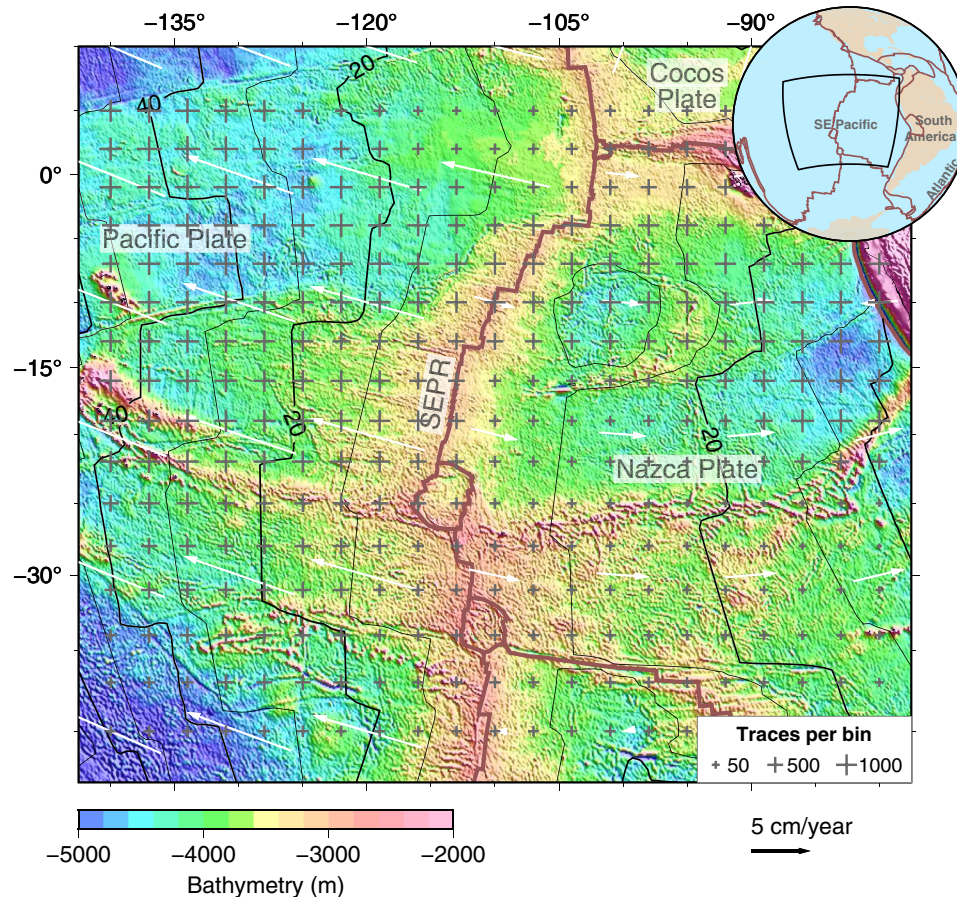


Fig. 1. Topography and tectonics of the SEPR and its surrounding oceans. The cap locations (gray crosses) are scaled by the number of records in each stack. The white arrows indicate the absolute plate motion, and their lengths reflect plate velocities in the spreading-aligned reference frame (72). The thick red lines in the center map denote the plate boundaries (73). The thin and thick black contours indicate seafloor age at 10- and 20-million years intervals, respectively (74). The black box in the inset map outlines the study region on a global scale.

radius. The stacked S410S and S660S precursors are migrated to depth after correction for move out, crustal thickness, and mantle heterogeneity (see Materials and Methods). The respective regional averages for the 410 and 660 are 415 ± 5 and 657 ± 6 km, producing a mean MTZ thickness of 242 ± 7 km (Fig. 2, A to C), which is comparable to the global average (22) and an earlier regional estimate (23). However, much of the SEPR is underlain by a thin MTZ due to up to 15-km depression of the 410 (Fig. 2A), which suggests along-ridge temperature variations extending into greater depths (24, 25). The most prominent feature of the MTZ structures is MTZ thickening beneath the Nazca Plate to the east of the SEPR, primarily due to a large depression (by as much as 20 km) of the 660 (Fig. 2C). On the basis of a cross section through this region (profile A-A'), the 410 below the northern segment of the SEPR is depressed by 4 ± 2 km, and the 660 is elevated by 6 ± 1 km, resulting in 10 ± 3 -km net MTZ thinning (Fig. 3A). The narrow MTZ overlaps with low S-wave velocities extending from the base of the MTZ to the surface. Toward the southern segment of the SEPR (along profile B-B'), the 410 remains depressed, and the undulations of the 660 correlate with those of the 410 (Fig. 3B). Further east, the 410 is slightly raised to 407 ± 8 km, and the reflection amplitudes of both precursors are noticeably reduced within a localized high-velocity zone with a

lateral dimension of 1500 km. A shallow 410, a deep 660, and high MTZ S-wave speeds are jointly consistent with a cold MTZ. The depth observations are robustly measured in both conventional common midpoint stacks and those enhanced by the FMSSA algorithm (fig. S2); however, the latter approach considerably reduces the data uncertainties (fig. S3). The observations are minimally affected by the tuning parameters of FMSSA upon further testing (fig. S4) and largely independent of the choice of tomographic correction model (fig. S5).

Our MTZ thickness measurements achieve a much higher lateral resolution than those of Flanagan and Shearer (26) from a similar approach (fig. S6B), due to the orders of magnitude increase in data volume over the past two decades (fig. S7) and, to a lesser extent, additional data cleaning by FMSSA. Our map offers more detail by reducing the stacking cap size from 10° radius to 5° . The main observations are comparable to recent global models (27, 28), although our increased dataset results in higher data density and smaller overall error (fig. S8). Despite these differences, all studies find a thickened MTZ beneath the Nazca Plate, with the exception of a $\sim 10^\circ$ northward shift of the observed location in the model of Waszek *et al.* (28). The thinning of the MTZ along the SEPR is also less pronounced in the two recent global models (fig. S6, C and D).

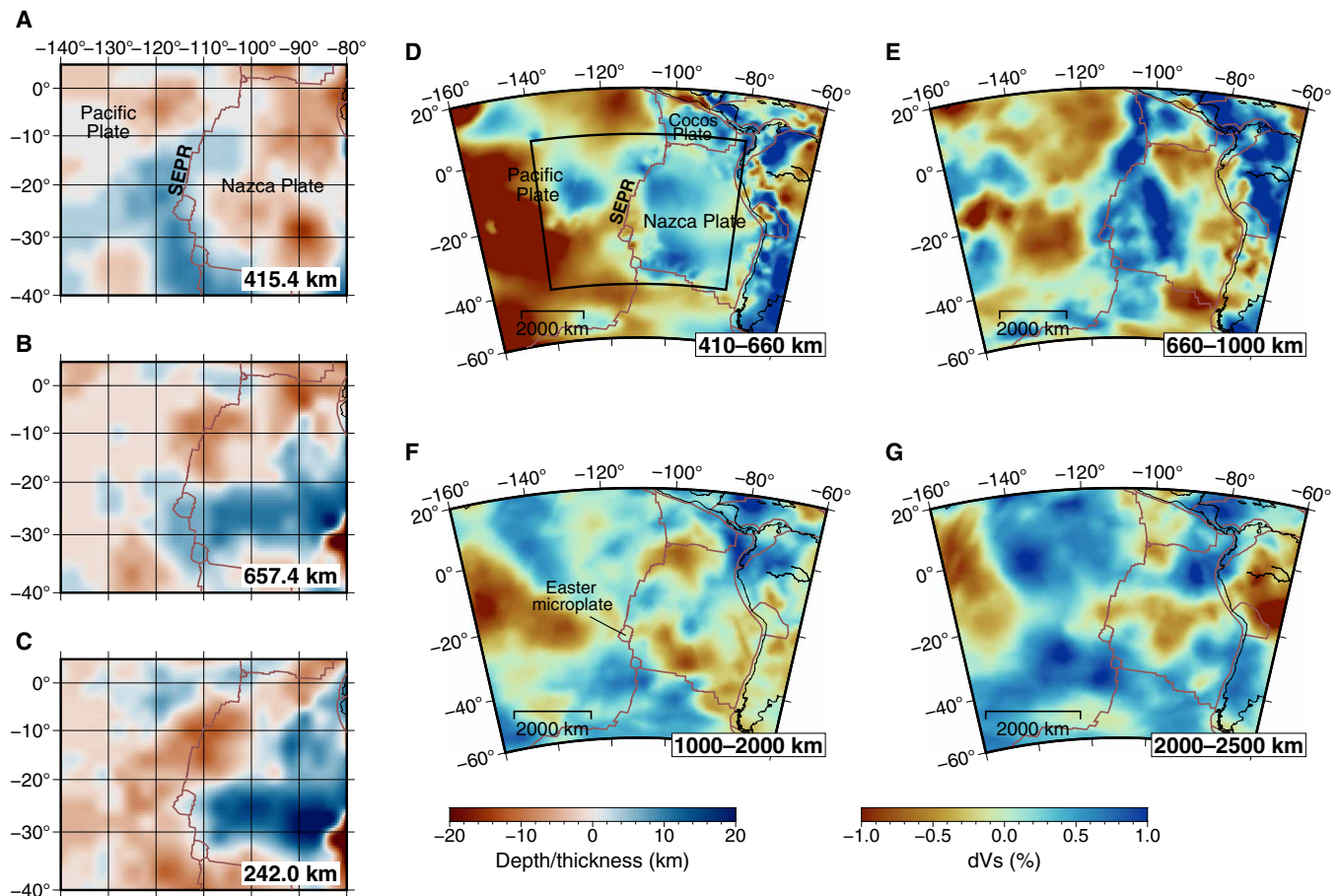


Fig. 2. Map of MTZ discontinuities and tomographic depth slices. (A to C) Topography of the 410 (A), the 660 (B), and transition zone thickness (C). The reconstruction adopts a rank cutoff value of $k = 30$. The depth estimates are shown relative to the regional average values at the bottom right corner of each panel. (D to G) The average S-wave velocity perturbations from the tomographic model LLNL-G3D-JPS (20) (D) between 410 and 660 km, (E) between 660 and 1000 km, (F) between 1000 and 2000 km, and (G) between 2000 and 2500 km. The brown lines denote the plate boundaries (73). The thick black box in (D) outlines the region where SS bounce points are located.

Tomographic evidence of ancient subduction

The MTZ thickening beneath the Nazca Plate reveals the possible presence of subduction that has gone unrecognized, despite slab-like, high S-wave velocity anomalies visible at depths from the MTZ (~400 km) to the lowermost mantle (~2600 km) in recent global tomographic images [e.g., LLNL-G3D-JPS (20)] (Fig. 2, D to G). Spatially, both the MTZ thickening and the velocity increase occur beneath the Nazca Plate. At midmantle depths, a continuous, high-velocity anomaly runs subparallel to the velocity anomaly that corresponds to the descending Nazca slab along the western margin of South America (Fig. 2E). In the lower mantle (>1000 km), the anomaly widens and begins to partition into two large but loosely connected segments near the Easter microplate (Fig. 2F). The influx of E-W oriented low-velocity anomalies, possibly originating from the Pacific LLSVP, is likely responsible for the gap (Fig. 2, F and G). The vertical continuity of the fast anomaly appears to form a westward dipping geometry that roughly mirrors the ongoing Nazca-South American plate convergence (Fig. 3C). The absence of overlying high velocities (in the upper mantle) suggests an old, possibly detached slab from the surface. The dip angle increases with depth and becomes nearly vertical before the high-velocity zone reaches the base of the mantle.

We note that existing tomographic models, which are derived largely from seismic travel times, exhibit great intermodel variability pertaining to the mantle structures beneath the eastern Pacific Ocean. To identify robust large-scale features, we compute vote maps for seven global models to examine regions of high and low S-wave velocities (see Materials and Methods). The faster-than-average vote results further confirm a dipping slab-like anomaly throughout the MTZ and lower mantle, with an offset distance of ~3000 km from the Nazca-South American convergent margin (Fig. 4, A and C). However, this high-velocity anomaly is only partially visible compared to the well-imaged Nazca slab. Another prominent feature of the vote maps is that many of the low-velocity structures are associated with the Pacific LLSVP (Fig. 4, B and D). The eastern arm of the LLSVP appears as a broad plume ascending from the core-mantle boundary, which is deflected toward the east and separated from the superswell anomaly.

DISCUSSION

Mesozoic-aged subduction in SE Panthalassa

If a paleoslab is responsible for our MTZ observations, then the spatial continuity of the westward-dipping high-velocity zone

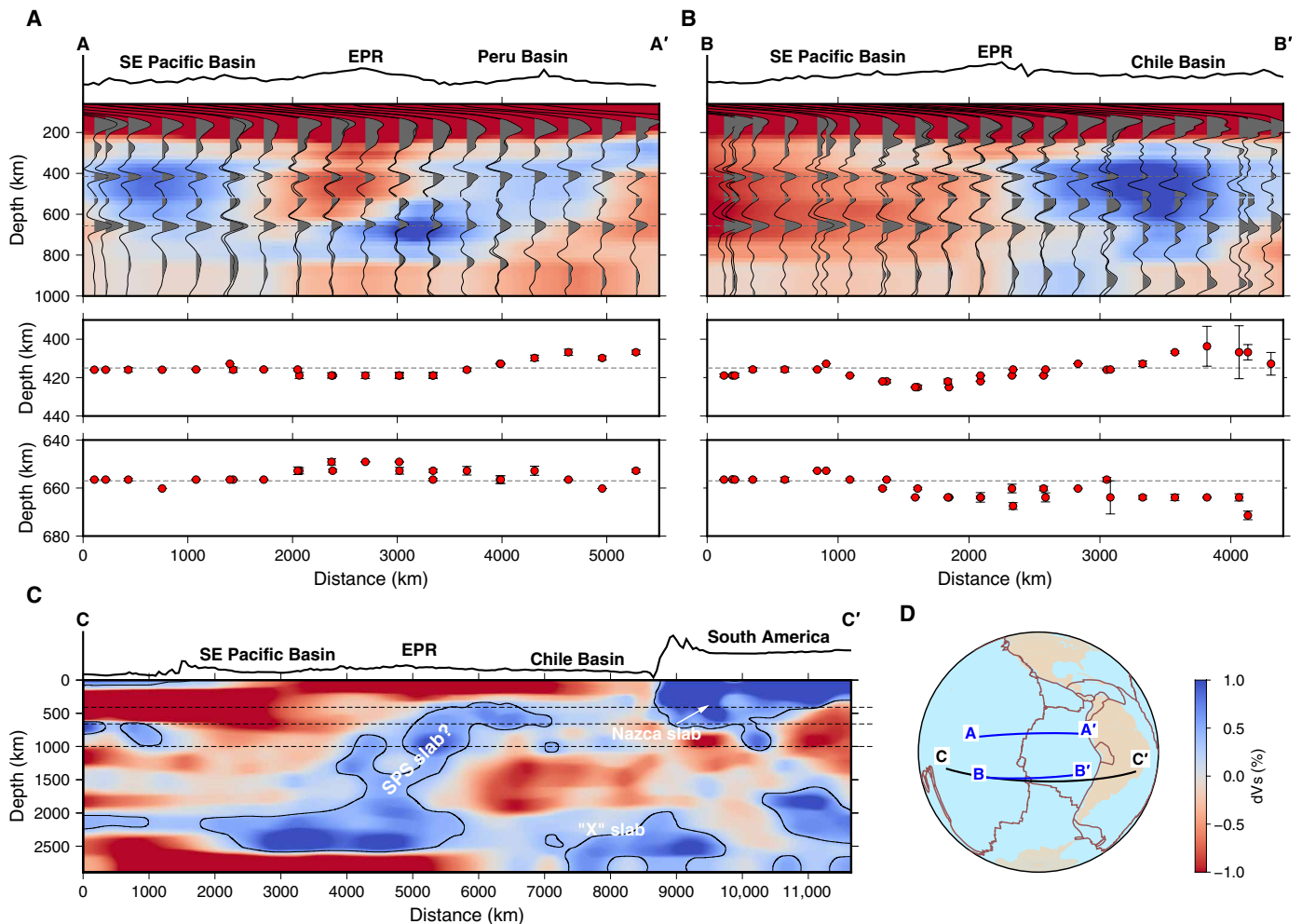


Fig. 3. Cross-sectional views of mantle velocities. (A and B) Cross sections along profiles A-A' and B-B' superimposed on the S-wave velocity perturbations from the GyPSuM model (49). The top panel shows the stacked SS waveforms with 95% confidence intervals from bootstrap resampling (black shaded areas below the curves). The bathymetry along the profile is plotted above the cross sections. The dashed lines represent the average depths of the 410 and 660. The bottom two panels below the tomographic cross sections are the expanded views of the discontinuity depths (with their respective SDs). (C) Whole-mantle depth cross section of S-wave velocity variations in model LLNL-G3D-JPS (20) along the great-circle path at 20°S (C-C'). The black lines indicate +0.4% velocity contour. The tomographic image is smoothed with median filtering. The bathymetry/topography along the profile is plotted above the cross section. The dashed lines indicate depths of 410, 660, and 1000 km. The "X" anomaly likely represents an ancient slab, but the detailed subduction process remains enigmatic (34). (D) Location of the cross sections in (A) to (C) with plate boundaries (brown lines) (73).

extending to the lowermost mantle would imply that the associated subduction event predates the current Nazca subduction. Such a subduction episode is absent from published subduction zone models, such as Slab2 (29). Before the Mesozoic, the two major subduction events in the present-day eastern Pacific Ocean include the subduction-induced closure of the Rheic Ocean and the advancement of the Patagonian Plate subduction zone (fig. S9) (30, 31). However, the relatively short duration of both episodes precludes a prolonged slab-mantle interaction that still affects the MTZ. The tomographically inferred subduction polarity is also opposite to that of the Patagonian Plate or the western Gondwana subduction zone, thus ruling out any correlation with the observed anomaly (see text S1).

High-velocity anomalies in seismic tomographic models are often overlooked candidates for slab remnants that fail to be incorporated

into current plate reconstruction models (21, 32). A reconstruction proposed by van der Meer *et al.* (21) that includes tomographic constraints identified several intraoceanic subduction zones surrounding the Panthalassa Ocean (paleo-Pacific) (fig. S10), including a Mesozoic-aged [between 250 and 240 million years ago (Ma)] divergent double subduction setting in the southeast [hereafter named the southeastern Panthalassa subduction (SPS)] (Fig. 5A). Their work suggests a marginal oceanic plate may have undergone a subduction reversal of the downward motion of the shorter segment of the slab (likely in the early Cretaceous). Upon the closure of the oceanic basin, the oceanic lithosphere was detached from the overlying surface. On the basis of our MTZ observations combined with tomography, we propose an alternative scenario that the Phoenix Plate must have been subducted beneath the Farallon Plate along an intraoceanic subduction zone initiated in the early Mesozoic (Fig. 5B).

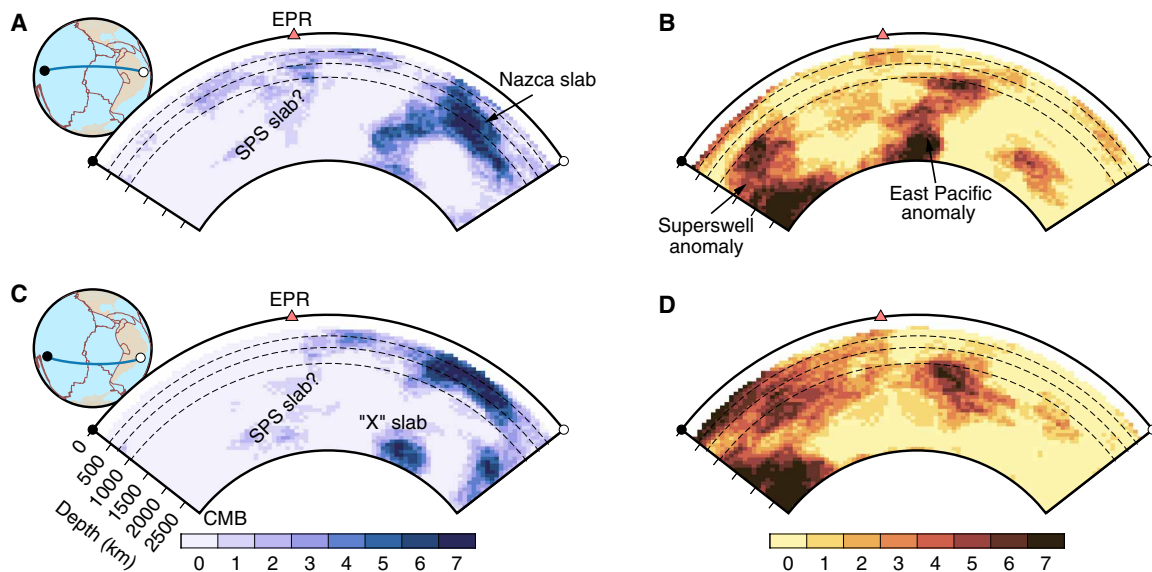


Fig. 4. Cross sections through tomographic velocity maps. (A and B) Seven S tomographic models are used for the W-E profiles through the northern part of our study area. (C and D) same as (A) and (B) for the southern part of our study area. The locations of the two profiles are shown in the inset maps of (A) and (C), respectively. Velocity maps in (A) and (C) identify vertically coherent fast regions that are common to the models, indicating the presence of subducted slabs, and (B) and (D) reveal vertically coherent slow regions in connection with hot upwelling material. The three dashed lines mark the depths of 410, 660, and 1000 km. CMB, core-mantle boundary.

This hypothesis predicts the consumption of the Phoenix Plate and the later-stage emergence of the Nazca Plate from the Farallon Plate. Following the eruption of the Ontong-Java-Manihiki-Hikurangi large igneous province at ~120 Ma, the Phoenix Plate fragmented into smaller plates and triggered the formation of the Chasca and Catequil Plates, as implied by satellite gravity data (33). The N-S directed Chasca-Catequil ridge spreading during the mid-to-late Cretaceous may inhibit the coexistence of an intraoceanic subduction along an E-W notable trench. Therefore, we conjecture that the SPS may have ceased its activity before the breakup of the Phoenix Plate (i.e., ~120 Ma). In addition, above the core-mantle boundary to the west of the Nazca subduction, the presence of a high-velocity anomaly (the “X” slab) on tomographic images (Figs. 3C and 4C) suggests either (i) a highly folded and deformed SPS slab that initially had an eastern segment but was later fragmented or (ii) a more complicated tectonic history involving a separate subduction event preceding the SPS episode (34).

The duration of the subducted SPS anomaly is corroborated by thermal history modeling, which shows that a low-temperature anomaly persists after a time span of 250 million years (Myr) (see text S2 and fig. S11). Given the temporal constraints, global correlations, assuming an average sinking velocity of 1.2 to 1.3 cm/year (35, 36), would suggest that the entire slab has already descended into the lower mantle. However, we observe that the slab remnants, comprising approximately 14% of the total slab volume, still accumulate in the MTZ after more than 100 Myr. This finding is incompatible with the global estimate (fig. S12) and suggests, instead, a decelerated sinking process with a rate of 0.5 cm/year in the upper mantle and 1.0 cm/year in the lower mantle (see text S3). The sinking rate within the MTZ is observed to be nearly half of that below it, indicating that the MTZ poses a strong barrier to mantle flow.

The MTZ structure beneath the SEPR is consistent with a remnant thermal anomaly from an intraoceanic subducted slab of

Mesozoic origin. Aside from a thermal origin, water transported into the MTZ by subduction could potentially perturb MTZ boundaries. The presence of 1 to 2 wt % of water in the MTZ would elevate the 410 and deepen the 660, thereby producing a thickened MTZ (27). However, our observation of increased velocities disfavors the contribution of hydration, which is expected to lower seismic velocities. Changes in major element chemistry would also affect discontinuity topography but cannot fully explain all seismic observations. For instance, increasing Al content during the majorite garnet to bridgmanite transformation primarily manifests itself in the depth of the 660 (37). Shifts in Fe content induce MTZ thickening but with large uncertainties in depth estimates due to limited experimental data on Fe-bearing mineral assemblages (38). Both scenarios require further constraints on Al or Fe concentrations in subduction settings, which currently remain largely unknown.

The recycling of cold oceanic lithosphere back into the deep mantle is not likely caused by delamination or dripping of the overlying lithosphere, a process that commonly occurs in continental regions (39, 40). If present, then a delaminated lithosphere provides a possible explanation for increased seismic velocities and thermally induced phase boundary perturbations upon sinking into the MTZ. According to the delamination model, the lithospheric removal predicts concurrent crustal thickening and surface uplift (41), which are absent in seismic observations (42). The observed negative dynamic topography in this region (43) is further at odds with the model of lithospheric delamination.

Implications for lower mantle structures

The presence of slab remnants subducted during the Mesozoic in the MTZ supports a segregated whole-mantle mixing model driven by a sharp local viscosity contrast between the upper and lower mantle (44, 45). The viscosity increase may be attributed to large, intrinsically

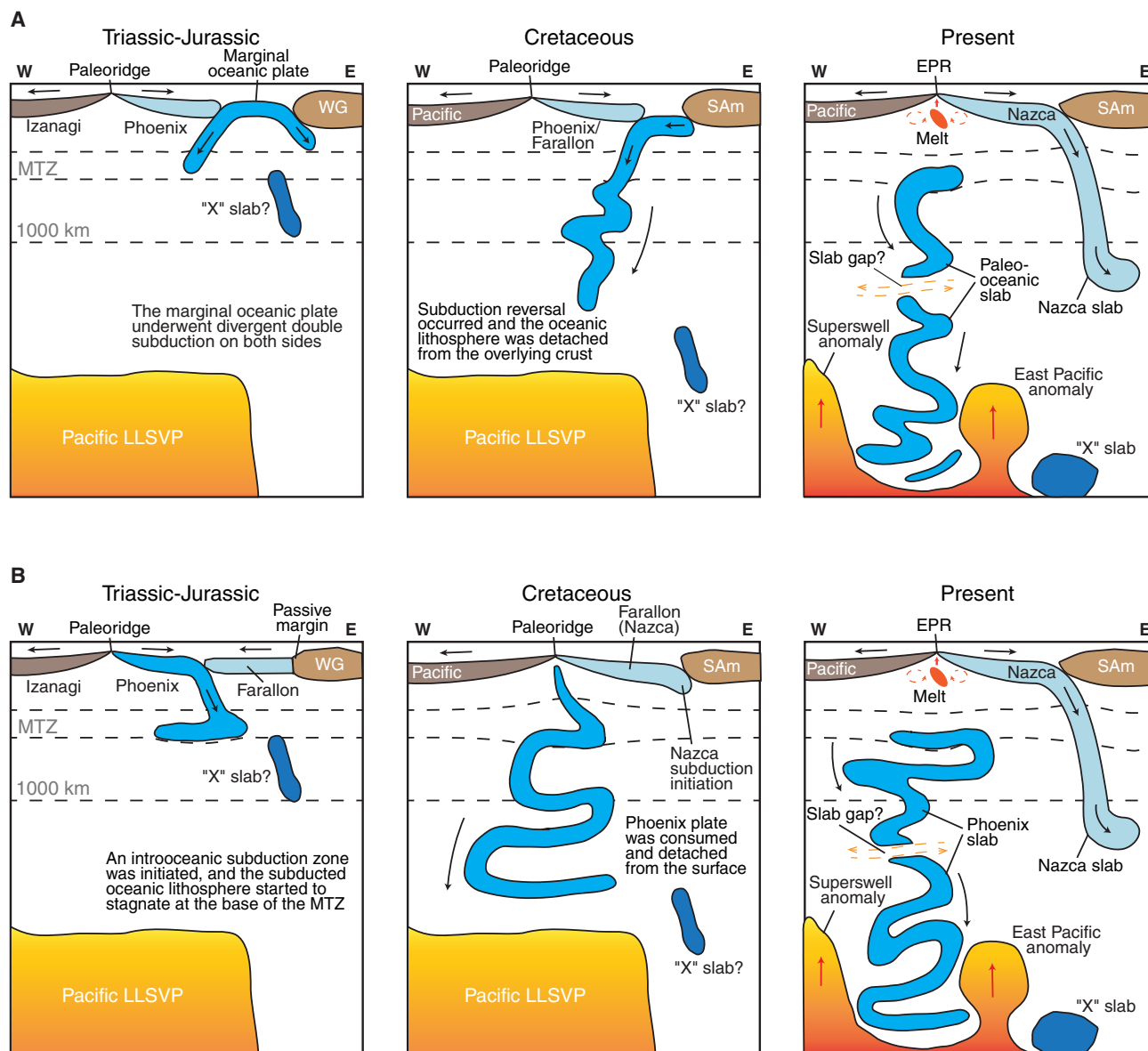


Fig. 5. Interpreted evolution of the SEPR anomaly. (A) The initiation of a divergent double subduction beneath the Phoenix Plate (west) and western Gondwana (WG; east) during the Triassic was followed by a subduction reversal of its western branch in the early Cretaceous, which was accompanied by the consumption of the oceanic basin. The Phoenix Plate broke up about 120 Ma, and the Farallon Plate captured some of the fragments and began to subduct underneath South America (SAm) (33). The deeply sinking oceanic slab impinges upon the Pacific LLSVP, separating it into two distinct anomalies. (B) The model predicts an intraoceanic subduction zone where the Phoenix Plate was subducted eastward under the Farallon Plate. In the late Cretaceous, the subducted oceanic slab was detached from the surface, which was roughly coincident with the onset of the Nazca subduction on the western margin of South America. The interaction between the Phoenix slab and the Pacific LLSVP has resulted in the separation of the superswell anomaly and the East Pacific anomaly. Both hypotheses suggest slab buckling in the lower mantle. The black dashed lines mark major mantle discontinuities (410, 660, and 1000 km) with depth.

viscous reservoirs in the midmantle, such as bridgmanite-enriched ancient mantle structures (6), which present a resistance to downgoing flow. Consequently, stagnation of slab material is promoted, resulting in a thickened MTZ.

Globally, regions of thickened MTZ show clear spatial correlations with locations of current subduction (28), with notable exceptions in eastern Siberia and the eastern Pacific Ocean east of the SEPR (Fig. 6). These regions have experienced relative subduction

quiescence over the past 150 Myr. In the former region, tomographic imaging provides evidence for Mesozoic subduction of the Mongol-Okhotsk Ocean underneath Siberia (46). Unlike this ocean-continent convergence without any influence from hot spots, the SPS is exceptional because of its direct impact on the Pacific LLSVP. As a result of the intraoceanic subduction, material from the eastern part of the Pacific LLSVP migrates along the bottom of the slab, bifurcating into the superswell anomaly and the eastern arm of the LLSVP. This

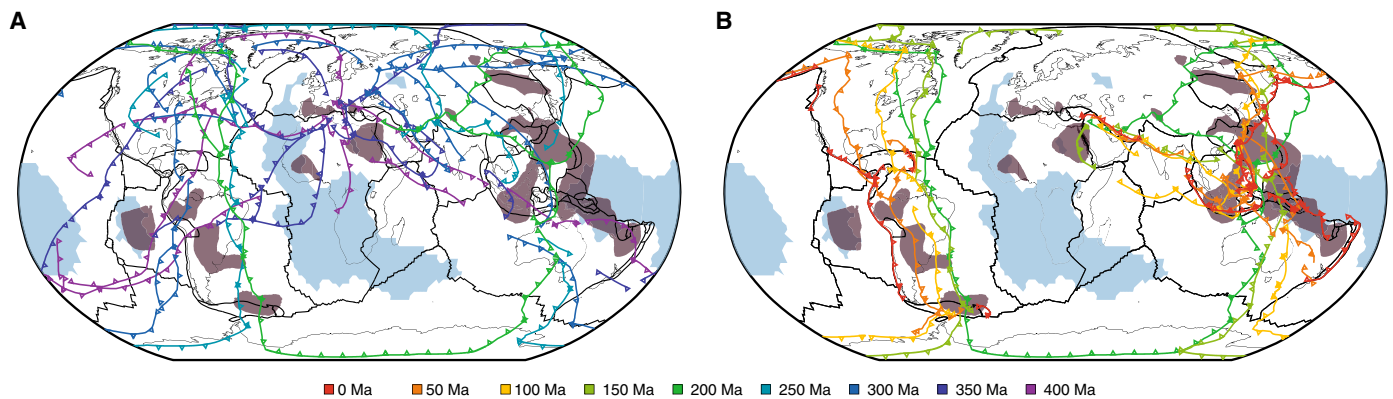


Fig. 6. The relationship between subduction locations, transition zone thickening, and LLSVP distribution. Modeled subduction zones since the late Paleozoic from Matthews *et al.* (31) at 50-Ma intervals for the period of (A) 0 to 200 Ma and (B) 200 to 400 Ma. The solid black lines represent the current plate boundaries (73). The blue shades outline the value of five in the vote maps of cluster analysis of lower mantle S-wave velocity profiles (1000 to 2800 km) (75), highlighting the geographical extent of the LLSVPs. The brown shades show positive (>10 km) anomalies of MTZ thickness (28). Most of the areas with a thickened MTZ are associated with ongoing subduction. The MTZ thickening beneath the Nazca Plate is unique because the proposed ancient subducted slab has been well preserved since the late Mesozoic and has direct interaction with the Pacific LLSVP in the lower mantle.

slab has apparently shaped the morphology of the LLSVP, as suggested by geodynamic models where “piles” are swept away from and sometimes split by downwelling slabs (47, 48). This is supported by seismic observations of circum-Pacific high-velocity anomalies in the lowermost mantle (1, 7, 49). The interaction between the piles and slabs is largely influenced by their physical properties, particularly the buoyancy and viscosity contrast (50, 51). The presence of cold, negatively buoyant slabs would impose substantial stresses on the LLSVP due to the gravitational instability and high viscosity of subducted material, which may induce strong topography (52) or varying LLSVP heights (48).

The inferred Triassic–Jurassic SPS reconciles the observations of the anomalous MTZ thickening and seismic tomography. Portions of the subducted lithosphere appear to be trapped in the MTZ, although the slab has penetrated to the lower mantle. A caveat is the absence of observations of volcanic arc terranes along a paleotrench, which may be explained by the Chasca–Catequil ridge collision that resulted in the subduction of several ridges beneath South America (53). The exact timing of the SPS is also open for debate and warrants further geological or geophysical investigations. Despite these uncertainties, our study combines seismic waveforms and tomographic models to shed light on the association between subduction history and deep Earth structure. Such an integrated approach, as used in this study, provides an independent method for recognizing possible ocean–ocean subduction zones that are traditionally difficult to detect. The observations place additional constraints on slab control of the shape of the LLSVP and bear important implications for future plate reconstructions.

MATERIALS AND METHODS

SS precursor dataset

We build a regional dataset by collecting all available broadband seismograms recorded before 2022 from the Incorporated Research Institutions for Seismology (IRIS) Data Management Center for SS bounce points located in the area defined by 40°S to 5°N and 140° to 80°W (Fig. 1 and fig. S1B). We retain earthquakes with depths less

than 75 km to minimize the interference from depth phases and magnitudes between 5.5 and 7.0 to ensure sufficient reflection amplitudes. The epicentral distance is restricted to 100° to 170°. We apply a Butterworth band-pass filter with corner periods at 15 and 75 s after rotating the seismograms into transverse components and downsampling to 1 Hz. Traces with a signal-to-noise ratio lower than 3.0 are discarded. The signal-to-noise ratio is defined as the ratio of the maximum amplitude of the SS main phase window [± 50 s centered on the predicted SS arrival from the preliminary reference Earth model (PREM) (54)] to that of the precursory window (50 s before the predicted S660S to 50 s after the predicted S410S arrival). Each trace is then normalized to unit amplitude, and the polarity is reversed if necessary. Our final dataset consists of 34,147 traces from 3437 events.

Data preconditioning

To explore the lateral variations of the 410 and 660, we partition the data into 336 overlapping circular caps with a radius of 5°. A move-out correction is applied to each seismogram to correct for the distance dependence of the SS-SdS differential times for a source–receiver distance of 130°. Because of the low amplitude nature of SS precursors, additional signal enhancement is typically required to bring energy reflected from mantle interfaces out of background noise. Instead of stacking all traces within each cap, we precondition the data subset (i.e., common midpoint gather of each cap) by partially stacking reflections within a 5° distance window (55, 56).

Seismic data reconstruction via matrix rank reduction

The nonuniform distribution of SS bounce points poses a common challenge in processing SS precursors. To simultaneously recover irregularly missing traces in the presence of noise, one potential approach involves the implementation of matrix rank reduction. Rank reduction–based methods assume that the data are predictable in space and treat data reconstruction and denoising as a low-rank approximation problem. The MSSA (57), a widely applied technique for rank reduction, facilitates this process by embedding

spatial data at a given temporal frequency into a trajectory matrix (i.e., a Hankel matrix).

The presence of both noisy and subsampled data can corrupt the low-rank structure of seismic data. Simultaneous denoising and reconstruction can be accomplished by minimizing a cost function with a low-rank constraint. In this study, to enhance weak signals while suppressing high-amplitude coherent (non-Gaussian) noise, instead of using the ℓ_2 norm for the data misfit term, we adopt a robust norm for the optimization problem with the following expression

$$J = \|\mathbf{u} - \mathcal{R}\mathbf{d}\|_\rho \text{ subject to } \text{rank}(\mathbf{d}) \leq k \quad (1)$$

where \mathbf{u} is the observed data, \mathbf{d} is the data after reconstruction and denoising, $\|\cdot\|_\rho$ denotes the robust norm, and ρ is Tukey's biweight loss function (58). The forward interpolation operator \mathcal{R} maps the data from the desired regular grid to the observed irregular grid, and its adjoint operator \mathcal{R}^* connects the observations to the gridded data (59, 60). A projected gradient descent algorithm (61) is introduced to iteratively solve the cost function

$$\mathbf{d}^{k+1} = \mathcal{P} \left[\mathbf{d}^k - \lambda \mathcal{R}^* \mathbf{W} (\mathcal{R} \mathbf{d}^k - \mathbf{u}) \right] \quad (2)$$

where \mathcal{P} is the projection operator, which represents the MSSA rank reduction filter, and λ is the step size; \mathbf{W} defines a diagonal matrix for Tukey's biweight loss function, and the elements of \mathbf{W} are given by

$$\mathbf{W}_{ii} = \begin{cases} \left[1 - \left(\frac{|\mathbf{r}_i|}{\beta} \right)^2 \right]^2, & |\mathbf{r}_i| \leq \beta \\ 0, & |\mathbf{r}_i| > \beta \end{cases} \quad (3)$$

where \mathbf{r}_i denotes the elements of the data misfit term $\mathbf{r} = \mathbf{u} - \mathcal{R}\mathbf{d}$ and β is a user-defined tuning parameter that controls the level of robustness of the MSSA filter.

We implement the FMSSA filter (62) as the projection operator to handle the three-dimensional precursor data. Compared with the classical algorithm, the FMSSA offers substantial computational savings by using random projections and avoiding the construction of block Hankel matrices. An example of FMSSA-filtered common midpoint gather is shown in fig. S13.

Synthetic test

We perform two tests to show that the observations are robust after simultaneous reconstruction and denoising. In the first test, we randomly remove 10% of the traces in a move out-corrected synthetic common midpoint gather, which is also corrupted by multiple bad traces (erratic noise). The seismograms are generated for the PREM model using the reflectivity method (63). The FMSSA effectively eliminates the corrupted noise, while recovering the missing traces at far offsets (fig. S14). In the spike test, two topographic anomalies with +10- and -10-km perturbations relative to the 660 (670-km depth in PREM) are introduced, and corresponding synthetic waveforms are computed. We add 10% random Gaussian noise and contaminate 10% of the traces with erratic noise. We then map the depth variations using the common midpoint stacking and the actual SS bounce point distribution. The presence of Gaussian and erratic noise introduces noticeable artifacts in the output maps. The reprocessing of the data volume based on data preconditioning and the FMSSA greatly suppresses the imaging artifacts, resulting in a smoothed and denoised map (fig. S15).

Time-to-depth conversion

The accuracy of discontinuity depth estimates is strongly affected by variations in crustal thickness and upper mantle velocity structure. To account for the travel time biases, we apply poststack timing corrections by applying constant time shifts calculated from CRUST1.0 (64) and S40RTS (65) to each discontinuity phase. Each time shift corresponds to the median value of the travel time residuals of each prestack record with respect to PREM. The stacked traces are lastly converted from time to depth according to travel times predicted by PREM. The resulting stacks are subsequently subjected to a bootstrap resampling test (66) using 300 random data subsets to assess the robustness and depth uncertainty of each reflection. We compare the migration results using various tomographic models, and the first-order observations are in reasonable agreement (fig. S5). The choice of tomographic correction model introduces an additional error in the MTZ thickness of 3.4 km.

Tomographic vote maps

Vote maps are an effective way to identify common features of seismically fast and slow regions imaged by tomography. In this study, we use the implementation of Shephard *et al.* (67) and generate cross-sectional vote maps for seven selected global S-wave tomographic models, which include S40RTS (65), GyPSuM (49), S362ANI+M (68), savani (69), SPani (70), SEMUCB-WM1 (15), and TX2019slab (71).

Supplementary Materials

This PDF file includes:

Supplementary Texts S1 to S3

Figs. S1 to S15

References

REFERENCES AND NOTES

1. W. Su, R. L. Woodward, A. M. Dziewonski, Degree 12 model of shear velocity heterogeneity in the mantle. *J. Geophys. Res. Solid Earth* **99**, 6945–6980 (1994).
2. M. Ishii, J. Tromp, Normal-mode and free-air gravity constraints on lateral variations in velocity and density of Earth's mantle. *Science* **285**, 1231–1236 (1999).
3. Y. J. Gu, A. M. Dziewonski, W. Su, G. Ekström, Models of the mantle shear velocity and discontinuities in the pattern of lateral heterogeneities. *J. Geophys. Res. Solid Earth* **106**, 11169–11199 (2001).
4. E. J. Garnero, A. K. McNamara, Structure and dynamics of Earth's lower mantle. *Science* **320**, 626–628 (2008).
5. F. Deschamps, L. Cobden, P. J. Tackley, The primitive nature of large low shear-wave velocity provinces. *Earth Planet. Sci. Lett.* **349**, 198–208 (2012).
6. M. D. Ballmer, C. Houser, J. W. Hernlund, R. M. Wentzcovitch, K. Hirose, Persistence of strong silica-enriched domains in the Earth's lower mantle. *Nat. Geosci.* **10**, 236–240 (2017).
7. A. M. Dziewonski, V. Lekic, B. A. Romanowicz, Mantle anchor structure: An argument for bottom up tectonics. *Earth Planet. Sci. Lett.* **299**, 69–79 (2010).
8. S. Ni, E. Tan, M. Gurnis, D. Helmberger, Sharp sides to the African superplume. *Science* **296**, 1850–1852 (2002).
9. Y. He, L. Wen, Structural features and shear-velocity structure of the "Pacific anomaly". *J. Geophys. Res. Solid Earth* **114**, B02309 (2009).
10. A. McNamara, S. Zhong, Thermochemical structures beneath Africa and the Pacific Ocean. *Nature* **437**, 1136–1139 (2005).
11. D. J. Bower, M. Gurnis, M. Seton, Lower mantle structure from paleogeographically constrained dynamic Earth models. *Geochem. Geophys. Geosyst.* **14**, 44–63 (2012).
12. S. Zhong, M. L. Rudolph, On the temporal evolution of long-wavelength mantle structure of the Earth since the early Paleozoic. *Geochem. Geophys. Geosyst.* **16**, 1599–1615 (2015).
13. A. Davaille, B. Romanowicz, Deflating the LLSVPs: Bundles of mantle thermochemical plumes rather than thick stagnant "piles". *Tectonics* **39**, e2020TC006265 (2020).
14. G. Schubert, G. Masters, P. Olson, P. Tackley, Superplumes or plume clusters? *Phys. Earth Planet. Inter.* **146**, 147–162 (2004).
15. S. W. French, B. Romanowicz, Broad plumes rooted at the base of the Earth's mantle beneath major hotspots. *Nature* **525**, 95–99 (2015).

16. S. Cottaar, V. Lekic, Morphology of seismically slow lower-mantle structures. *Geophys. J. Int.* **207**, 1122–1136 (2016).
17. R. Montelli, G. Nole, F. A. Dahlen, G. Masters, E. R. Engdahl, S.-H. Hung, Finite-frequency tomography reveals a variety of plumes in the mantle. *Science* **303**, 338–343 (2004).
18. W. Lei, Y. Ruan, E. Bozdağ, D. Peter, M. Lefebvre, D. Komatitsch, J. Tromp, J. Hill, N. Podhorszki, D. Pugmire, Global adjoint tomography—Model GLAD-M25. *Geophys. J. Int.* **223**, 1–21 (2020).
19. A. Deuss, Global observations of mantle discontinuities using SS and PP precursors. *Surv. Geophys.* **30**, 301–326 (2009).
20. N. A. Simmons, S. C. Myers, G. Johannesson, E. Matzel, S. P. Grand, Evidence for long-lived subduction of an ancient tectonic plate beneath the southern Indian Ocean. *Geophys. Res. Lett.* **42**, 9270–9278 (2015).
21. D. G. van der Meer, T. H. Torsvik, W. Spakman, D. J. J. van Hinsbergen, M. L. Amaru, Intra-Panthalassa Ocean subduction zones revealed by fossil arcs and mantle structure. *Nat. Geosci.* **5**, 215–219 (2012).
22. Y. J. Gu, A. M. Dziewonski, Global variability of transition zone thickness. *J. Geophys. Res. Solid Earth* **107**, ESE2-1–ESE 2-17 (2002).
23. Y. Shen, A. F. Sheehan, K. G. Duerke, C. de Groot-Hedlin, H. Gilbert, Mantle discontinuity structure beneath the southern East Pacific Rise from P-to-S converted phases. *Science* **280**, 1232–1235 (1998).
24. C. A. Dalton, C. H. Langmuir, A. Gale, Geophysical and geochemical evidence for deep temperature variations beneath mid-ocean ridges. *Science* **344**, 80–83 (2014).
25. M. R. Agius, C. A. Rychert, N. Harmon, S. Tharimena, J.-M. Kendall, A thin mantle transition zone beneath the equatorial Mid-Atlantic ridge. *Nature* **589**, 562–566 (2021).
26. M. P. Flanagan, P. M. Shearer, Global mapping of topography on transition zone velocity discontinuities by stacking SS precursors. *J. Geophys. Res. Solid Earth* **103**, 2673–2692 (1998).
27. C. Houser, Global seismic data reveal little water in the mantle transition zone. *Earth Planet. Sci. Lett.* **448**, 94–101 (2016).
28. L. Waszek, B. Tauzin, N. C. Schmerr, M. D. Ballmer, J. C. Afonso, A poorly mixed mantle transition zone and its thermal state inferred from seismic waves. *Nat. Geosci.* **14**, 949–955 (2021).
29. G. P. Hayes, G. L. Moore, D. E. Portner, M. Hearne, H. Flamme, M. Furtney, G. M. Smoczyk, Slab2, a comprehensive subduction zone geometry model. *Science* **362**, 58–61 (2018).
30. M. Domeier, T. H. Torsvik, Plate tectonics in the late paleozoic. *Geosci. Front.* **5**, 303–350 (2014).
31. K. J. Matthews, K. T. Maloney, S. Zahirovic, S. E. Williams, M. Seton, R. D. Müller, Global plate boundary evolution and kinematics since the late paleozoic. *Glob. Planet. Change* **146**, 226–250 (2016).
32. K. Sigloch, M. G. Mihalynuk, Intra-oceanic subduction shaped the assembly of Cordilleran North America. *Nature* **496**, 50–56 (2013).
33. M. Seton, R. D. Müller, S. Zahirovic, C. Gaina, T. Torsvik, G. Shephard, A. Talsma, M. Gurnis, M. Turner, S. Maus, M. Chandler, Global continental and ocean basin reconstructions since 200Ma. *Earth Sci. Rev.* **113**, 212–270 (2012).
34. Y.-W. Chen, J. Wu, J. Suppe, Southward propagation of Nazca subduction along the Andes. *Nature* **565**, 441–447 (2019).
35. D. G. van der Meer, W. Spakman, D. J. van Hinsbergen, M. L. Amaru, T. H. Torsvik, Towards absolute plate motions constrained by lower-mantle slab remnants. *Nat. Geosci.* **3**, 36–40 (2010).
36. N. P. Butterworth, A. S. Talsma, R. D. Müller, M. Seton, H.-P. Bunge, B. S. A. Schubert, G. E. Shephard, C. Heine, Geological, tomographic, kinematic and geodynamic constraints on the dynamics of sinking slabs. *J. Geodyn.* **73**, 1–13 (2014).
37. D. J. Weidner, Y. Wang, Chemical- and clapeyron-induced buoyancy at the 660 km discontinuity. *J. Geophys. Res. Solid Earth* **103**, 7431–7441 (1998).
38. V. Thio, L. Cobden, J. Trampert, Seismic signature of a hydrous mantle transition zone. *Phys. Earth Planet. Inter.* **250**, 46–63 (2016).
39. P. Bird, Continental delamination and the colorado plateau. *J. Geophys. Res. Solid Earth* **84**, 7561–7571 (1979).
40. G. A. Houseman, D. P. McKenzie, P. Molnar, Convective instability of a thickened boundary layer and its relevance for the thermal evolution of continental convergent belts. *J. Geophys. Res. Solid Earth* **86**, 6115–6132 (1981).
41. O. H. Göğüş, R. N. Pysklywec, Near-surface diagnostics of dripping or delaminating lithosphere. *J. Geophys. Res. Solid Earth* **113**, B11404 (2008).
42. R. S. Detrick, A. J. Harding, G. M. Kent, J. A. Orcutt, J. C. Mutter, P. Buhl, Seismic structure of the southern East Pacific Rise. *Science* **259**, 499–503 (1993).
43. B. Steinberger, Effects of latent heat release at phase boundaries on flow in the Earth's mantle, phase boundary topography and dynamic topography at the Earth's surface. *Phys. Earth Planet. Inter.* **164**, 2–20 (2007).
44. M. D. Ballmer, N. C. Schmerr, T. Nakagawa, J. Ritsema, Compositional mantle layering revealed by slab stagnation at ~1000-km depth. *Sci. Adv.* **1**, e1500815 (2015).
45. M. L. Rudolph, V. Lekić, C. Lithgow-Bertelloni, Viscosity jump in Earth's mid-mantle. *Science* **350**, 1349–1352 (2015).
46. R. Van der Voo, W. Spakman, H. Bijwaard, Mesozoic subducted slabs under Siberia. *Nature* **397**, 246–249 (1999).
47. E. Tan, W. Leng, S. Zhong, M. Gurnis, On the location of plumes and lateral movement of thermochemical structures with high bulk modulus in the 3-D compressible mantle. *Geochem. Geophys. Geosyst.* **12**, Q07005 (2011).
48. Q. Yuan, M. Li, Vastly different heights of LLVPs caused by different strengths of historical slab push. *Geophys. Res. Lett.* **49**, e2022GL099564 (2022).
49. N. A. Simmons, A. M. Forte, L. Boschi, S. P. Grand, GyPSuM: A joint tomographic model of mantle density and seismic wave speeds. *J. Geophys. Res. Solid Earth* **115**, 2010JB007631 (2010).
50. F. Deschamps, P. J. Tackley, Searching for models of thermo-chemical convection that explain probabilistic tomography: I. Principles and influence of rheological parameters. *Phys. Earth Planet. Inter.* **171**, 357–373 (2008).
51. F. Deschamps, P. J. Tackley, Searching for models of thermo-chemical convection that explain probabilistic tomography. II—Influence of physical and compositional parameters. *Phys. Earth Planet. Inter.* **176**, 1–18 (2009).
52. L. H. Kellogg, B. H. Hager, R. D. van der Hilst, Compositional stratification in the deep mantle. *Science* **283**, 1881–1884 (1999).
53. G. Gianni, C. Navarrete, D. Orts, J. Tobal, A. Folguera, M. Giménez, Patagonian broken foreland and related synorogenic rifting: The origin of the chubut group basin. *Tectonophysics* **649**, 81–99 (2015).
54. A. M. Dziewonski, D. L. Anderson, Preliminary reference Earth model. *Phys. Earth Planet. Inter.* **25**, 297–356 (1981).
55. Y. J. Gu, M. Sacchi, Radon transform methods and their applications in mapping mantle reflectivity structure. *Surv. Geophys.* **30**, 327–354 (2009).
56. R. Schultz, Y. J. Gu, Multiresolution imaging of mantle reflectivity structure using SS and P'P' precursors. *Geophys. J. Int.* **195**, 668–683 (2013).
57. V. Oropeza, M. Sacchi, Simultaneous seismic data denoising and reconstruction via multichannel singular spectrum analysis. *Geophysics* **76**, V25–V32 (2011).
58. A. E. Beaton, J. W. Tukey, The fitting of power series, meaning polynomials, illustrated on band-spectroscopic data. *Technometrics* **16**, 147–185 (1974).
59. F. Carozzi, M. D. Sacchi, Interpolated multichannel singular spectrum analysis: A reconstruction method that honors true trace coordinates. *Geophysics* **86**, V55–V70 (2021).
60. R. Lin, Y. Guo, F. Carozzi, M. D. Sacchi, Simultaneous deblending and source reconstruction for compressive 3D simultaneous-source acquisition data via interpolated multichannel singular spectrum analysis. *Geophysics* **87**, V559–V570 (2022).
61. R. Lin, B. Bahia, M. D. Sacchi, Iterative deblending of simultaneous-source seismic data via a robust singular spectrum analysis filter. *IEEE Trans. Geosci. Remote Sens.* **60**, 1–10 (2021).
62. J. Cheng, M. Sacchi, J. Gao, Computational efficient multidimensional singular spectrum analysis for prestack seismic data reconstruction. *Geophysics* **84**, V111–V119 (2019).
63. K. Fuchs, G. Müller, Computation of synthetic seismograms with the reflectivity method and comparison with observations. *Geophys. J. Int.* **23**, 417–433 (1971).
64. G. Laske, G. Masters, Z. Ma, M. Pasyanos, Update on CRUST1.0 - A 1-degree global model of Earth's crust. *Geophys. Res. Abstr.* **15**, 2658 (2013).
65. J. Ritsema, A. A. Deuss, H. J. van Heijst, J. H. Woodhouse, S40RTS: A degree-40 shear-velocity model for the mantle from new Rayleigh wave dispersion, teleseismic traveltimes and normal-mode splitting function measurements. *Geophys. J. Int.* **184**, 1223–1236 (2011).
66. B. Efron, R. Tibshirani, Statistical data analysis in the computer age. *Science* **253**, 390–395 (1991).
67. G. E. Shephard, C. Houser, J. W. Hernlund, J. J. Valencia-Cardona, R. G. Trønnes, R. M. Wentzcovitch, Seismological expression of the iron spin crossover in ferropericlasite in the Earth's lower mantle. *Nat. Commun.* **12**, 5905 (2021).
68. P. Moulik, G. Ekström, An anisotropic shear velocity model of the Earth's mantle using normal modes, body waves, surface waves and long-period waveforms. *Geophys. J. Int.* **199**, 1713–1738 (2014).
69. L. Auer, L. Boschi, T. W. Becker, T. Nissen-Meyer, D. Giardini, *Savani*: A variable resolution whole-mantle model of anisotropic shear velocity variations based on multiple data sets. *J. Geophys. Res. Solid Earth* **119**, 3006–3034 (2014).
70. A. Tesoniero, L. Auer, L. Boschi, F. Cammarano, Hydration of marginal basins and compositional variations within the continental lithospheric mantle inferred from a new global model of shear and compressional velocity. *J. Geophys. Res. Solid Earth* **120**, 7789–7813 (2015).
71. C. Lu, S. P. Grand, H. Lai, E. J. Garnero, TX2019slab: A new P and S tomography model incorporating subducting slabs. *J. Geophys. Res. Solid Earth* **124**, 11549–11567 (2019).
72. T. W. Becker, A. J. Schaeffer, S. Lebedev, C. P. Conrad, Toward a generalized plate motion reference frame. *Geophys. Res. Lett.* **42**, 3188–3196 (2015).
73. P. Bird, An updated digital model of plate boundaries. *Geochem. Geophys. Geosyst.* **4**, 1027 (2003).

74. M. Seton, R. D. Müller, S. Zahirovic, S. Williams, N. M. Wright, J. Cannon, J. M. Whittaker, K. J. Matthews, R. McGirr, A global data set of present-day oceanic crustal age and seafloor spreading parameters. *Geochem. Geophys. Geosyst.* **21**, e2020GC009214 (2020).
75. V. Lekic, S. Cottaar, A. Dziewonski, B. Romanowicz, Cluster analysis of global lower mantle tomography: A new class of structure and implications for chemical heterogeneity. *Earth Planet. Sci. Lett.* **357**, 68–77 (2012).
76. R. D. Müller, J. Cannon, X. Qin, R. J. Watson, M. Gurnis, S. Williams, T. Pfaffelmoser, M. Seton, S. H. J. Russell, S. Zahirovic, GPlates: Building a virtual earth through deep time. *Geochem. Geophys. Geosyst.* **19**, 2243–2261 (2018).
77. J. B. Murphy, J. D. Keppie, R. D. Nance, J. Dostal, Comparative evolution of the iapetus and rheic oceans: A North America perspective. *Gondw. Res.* **17**, 482–499 (2010).
78. R. D. Nance, G. Gutiérrez-Alonso, J. D. Keppie, U. Linnemann, J. B. Murphy, C. Quesada, R. A. Strachan, N. H. Woodcock, Evolution of the rheic ocean. *Gondw. Res.* **17**, 194–222 (2010).
79. H. Bahlburg, F. Hervé, Geodynamic evolution and tectonostratigraphic terranes of northwestern Argentina and northern Chile. *Geol. Soc. Am. Bull.* **109**, 869–884 (1997).
80. V. A. Ramos, Patagonia: A paleozoic continent adrift? *J. South Am. Earth Sci.* **26**, 235–251 (2008).
81. D. Turcotte, G. Schubert, “Heat transfer” in *Geodynamics* (Cambridge Univ. Press, ed. 3, 2014), pp. 160–229.
82. F. Cammarano, S. Goes, P. Vacher, D. Giardini, Inferring upper-mantle temperatures from seismic velocities. *Phys. Earth Planet. Inter.* **138**, 197–222 (2003).
83. E. Hafkenscheid, M. J. R. Wortel, W. Spakman, Subduction history of the Tethyan region derived from seismic tomography and tectonic reconstructions. *J. Geophys. Res. Solid Earth* **111**, B08401 (2006).
84. D. G. van der Meer, D. J. J. van Hinsbergen, W. Spakman, Atlas of the underworld: Slab remnants in the mantle, their sinking history, and a new outlook on lower mantle viscosity. *Tectonophysics* **723**, 309–448 (2018).
85. M. East, R. D. Müller, S. Williams, S. Zahirovic, C. Heine, Subduction history reveals cretaceous slab superflux as a possible cause for the mid-cretaceous plume pulse and superswell events. *Gondw. Res.* **79**, 125–139 (2020).
86. R. D. Müller, M. Seton, S. Zahirovic, S. E. Williams, K. J. Matthews, N. M. Wright, G. E. Shephard, K. T. Maloney, N. Barnett-Moore, M. Hosseinpour, D. J. Bower, J. Cannon, Ocean basin evolution and global-scale plate reorganization events since pangea breakup. *Annu. Rev. Earth Planet. Sci.* **44**, 107–138 (2016).
87. N. A. Simmons, A. M. Forte, S. P. Grand, Thermochemical structure and dynamics of the African superplume. *Geophys. Res. Lett.* **34**, 2006GL028009 (2007).
88. J. Ritsema, H. J. van Heijst, J. H. Woodhouse, Complex shear wave velocity structure imaged beneath Africa and Iceland. *Science* **286**, 1925–1928 (1999).
89. T. H. Torsvik, B. Steinberger, G. E. Shephard, P. V. Doubrovine, C. Gaina, M. Domeier, C. P. Conrad, W. W. Sager, Pacific-panthalassic reconstructions: Overview, errata and the way forward. *Geochem. Geophys. Geosyst.* **20**, 3659–3689 (2019).

Acknowledgments: We thank M. Sacchi for discussions on seismic signal processing and D. van Hinsbergen for discussions on tectonic interpretation. We also thank D. van der Meer for sharing plate reconstruction models and C. Houser for providing discontinuity depth measurements. Comments from the reviewers were helpful. **Funding:** J.W., V.L., and N.C.S. acknowledge support from NASA SSERVI Cooperative Agreement 80NSSC19M0216. Y.J.G. is supported by Natural Sciences and Engineering Research Council of Canada and Future Energy Systems of the University of Alberta. **Author contributions:** J.W. and V.L. conceived the project. J.W. performed all analyses with the support of R.L. on seismic data processing and Y.J.G. on data curation. R.L. and Y.G. developed the FMSSA algorithm. V.L. and N.C.S. contributed to the interpretation of the results. J.W., V.L., and N.C.S. shaped the scope of the study. All authors contributed to writing the manuscript. **Competing interests:** The authors declare that they have no competing interests. **Data and materials availability:** All data needed to evaluate the conclusions in the paper are present in the paper and/or the Supplementary Materials. Raw seismic data are downloaded from the IRIS Data Management Center (<https://ds.iris.edu/ds/nodes/dmc/>). The MTZ topography model is available at the Digital Repository at the University of Maryland: <http://hdl.handle.net/1903/31563>. The LLNL-G3D-JPS model is available at <https://gs.llnl.gov/nuclear-threat-reduction/nuclear-explosion-monitoring/global-3d-seismic-tomography>. The tomographic vote maps can be visualized via SubMachine at <https://users.earth.ox.ac.uk/~smachine/cgi/index.php>. The plate reconstruction models are accessed using GPlates (76).

Submitted 17 January 2024
Accepted 22 August 2024
Published 27 September 2024
10.1126/sciadv.ado1219